Chapter 2: **EXPERIMENTAL TECHNIQUES**

In this Chapter we summarise the main experimental techniques we used for this Thesis. We give a detailed description of the theoretical fundamentals of each technique, paying special attention to those to which we made some changes in the form of measurement. We also give a detailed description of the experimental equipment, with precise descriptions and schematic views of the systems we used to measure the spectroscopic and non-linear optical properties. The experimental techniques outlined in this Chapter are available at the Rovira i Virgili University and also at other universities in Spain (the University of Barcelona and the University of the Basque Country) and in France (the Joseph Fourier University in Grenoble and the Claude Bernard University in Lyon, as well as at various research centres such as the Institute Laue-Langevin in Grenoble).

2.1. Crystal growth technique: Top-Seeded Solution Growth.

Top-Seeded Solution Growth (TSSG) is a flux growth technique commonly used to grow crystals from high temperature solutions. Flux growth methods allow the crystals to grow before the melting temperature is reached and are used when the crystals melt incongruently or when there is a phase transition before melting. The components of the final desired materials are dissolved in a solvent. The difference between TSSG and other flux techniques is that crystals grow in a crystal seed placed in contact with the surface of the solution. With this technique, when the solution is cooled slowly, the crystal starts to grow in the supersaturated melt and continues to grow while the temperature decreases steadily. Inclusion-free single crystals of a size that is suitable for optical investigations can be obtained. To avoid secondary nucleation, the crystal seed should be at the coldest spot in the flux and good convection must be achieved either by rotating either of the crystal or the crucible. In this Thesis we only rotated the crystal. The direction of the rotation should be periodically reversed to avoid asymmetrical flow rates and flux inhomogenity.[160]

High quality large single crystals of the KTP family can be grown in a single-zone furnace (see Figure 1 in *paper II*), as Cheng et al.[161] have already demonstrated. Depending on the slow-cooling program we used, the furnace was controlled by a Eurotherm 818P or a Eurotherm 902 controller/programmer, connected to an S-type thermocouple Pt / Pt - Rh 10 %. This thermocouple was placed near the resistances, in the central zone of the furnace to ensure stable and reliable measurement of the temperature. The controller was also connected to a thyristor to control the power of the furnace by cutting the a.w. wavelength. These furnaces were available at the FiCMA (*Física i Cristal·lografia de Materials group*) of the Rovira i Virgili University in Tarragona (Spain).

A typical characterisation of the thermal gradient of the furnace involves determining its axial and radial gradients to identify the best location for the platinum crucible inside the furnace. Another important thermal gradient is the one inside the solution, which is different from the one for the empty furnace because of the platinum crucible and the solution. We used a low temperature gradient inside the growth solution for RTP crystals (see *paper II*).

The crucible is supported inside the furnace by an alumina column that can be manually displaced to position the crucible in the right zone of the furnace (see Figure 1 in *paper II*). We used pure platinum crucibles of 25 cm^3 (used in the experiments to determine the crystallisation regions and in the preliminary crystal growth experiments; see Chapter 3) and 125 cm^3 (used in the single crystal growth experiments; see Chapter 5). The reactivity of platinum with the oxides used as the starting materials for growing $RbTiOPO_4$ is null, so the platinum does not contaminate the crystals.

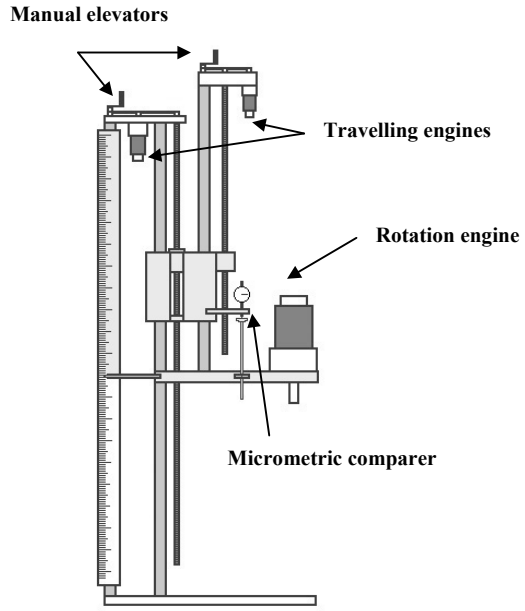

Figure 2.1. *Metallic structure to support, vertically displace and rotate the crystal seed.*

Figure 2.1 shows the mechanical part of the crystal growth system. It comprises a vertical metal structure that is extremely rigid and stable and that allows vertical displacement and rotation of the crystal seed. The crystal seed is attached to an alumina rod laced with Pt wire. We used a Mitutoyo comparer to measure the position of the crystal seed to an accuracy of 0.01 mm in order to accurately determine the saturation temperature.

2.2. Cutting and polishing the single-crystal samples: techniques and experimental equipment.

When characterising the optical materials, the samples must be adequately prepared. We used a goniometer to orientate the crystal and then cut the samples with a Struers Minitom diamond saw with disks of between 0.12 and 0.25 mm in thickness.

The samples were then polished in a Logytech PM5 polisher with an oscillatory arm that allowed us to accurately rotate and pressurise the samples, depending on the hardness of the material to be polished. We used two kinds of abrasive substances: alumina powders (hardness = 7 mohs) or diamond powders, depending on the quality of the polish required. We measured the quality of the polish using parameters such as roughness, flatness (measured by a self-collimator) and parallelism between opposite faces of the sample (measured by the same self-collimator using the two reflections on the opposite faces of the sample). These systems are available at the FiCMA.

The first step in the cutting and polishing process for a sample of RTP or one of its isostructurals was to polish a plane normal to the [001] direction by inserting the sample in a piece of

aluminium cut at the angle between the (201) and $(\bar{2}01)$ faces (62.4º). We then verified the orientation of this plane by texture analysis using a Siemens D-5000 X-ray diffractometer equipped with an open Euler ring working with Schulz geometry. This is available at the *Servei de Recursos Científics* of the Rovira i Virgili University. The orientation of the sample is defined by three angles with respect to the diffraction plane: the complementary incident angle (ω), the rotation angle between the intersection of the plane of the sample and the plane of diffraction (χ), and the rotation angle around the normal axis to the plane of the sample (φ). Our first analysis involved a pole figure of the (004) plane. This analysis comprised χ (0 → 24º) and φ (0 → 360º) scans with $\Delta\chi = 2º$ and $\Delta\varphi = 3º$ for a given 2θ angle. In this case, this was the angle corresponding to the diffraction of the (004) plane (33.854º). Figure 2.2 plots the intensities measured by the diffractometer in a stereographic projection with level lines (pole figure).

These results confirm that the polished plane is perpendicular to the [001] direction. We then did a pole figure of the (404) plane for a 2θ = 44.188º, χ = 20 → 56º and φ = 0 → 360. In this family of crystals, the fact that $\boldsymbol{a} \approx 2\boldsymbol{b}$ makes it difficult to orient the sample because the 2θ angles of the (2*h*0*l*) and the (0*hl*) planes practically coincide. As we can see in Figure 2.3, the pole figure of the (404) plane not only shows the two peaks corresponding to the diffraction of this family of planes, but also the additional peaks corresponding to the (024) planes.

However, this coincidence means that we can orient the ***a*** and ***b*** directions, in just one measurement because, while the (012) plane is an extinction and the intensity of its peak (expected around 21º) will be very low, the (202) plane has a higher-intensity peak around the same position. Figure 2.4 shows the overlapping of these two 2θ scan. We can see that the peaks obtained at φ = 0 and 180º in the pole figure correspond to the (404) planes and the peaks obtained at φ = 90 and 270º correspond to the (024) plane.

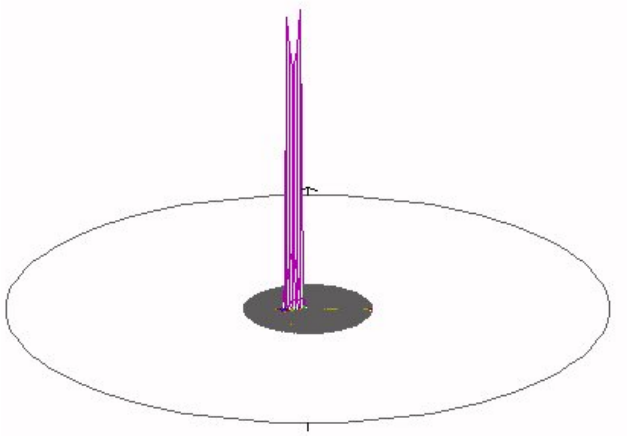

Figure 2.2. *Pole figure corresponding to the (004) plane with a 2θ = 33.854º; χ = 0 → 24º, and φ = 0 → 360º*

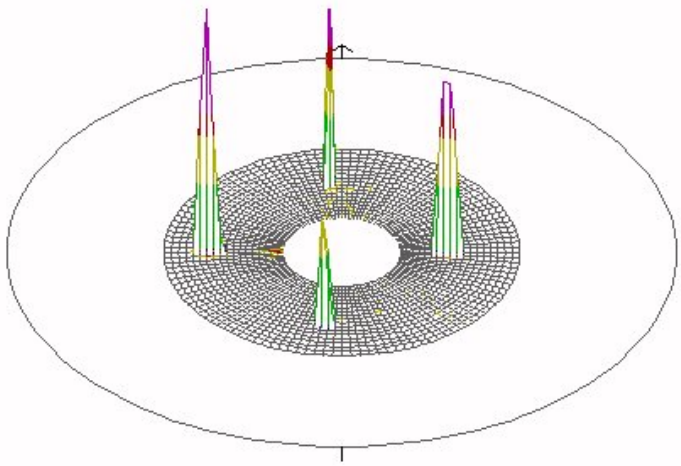

Figure 2.3. *Pole figure corresponding to the (404)/(024) planes with a 2θ = 44.188º; χ = 20 → 56º, and φ = 0 → 360º. The (χ,φ) positions are indicated in the figure.*

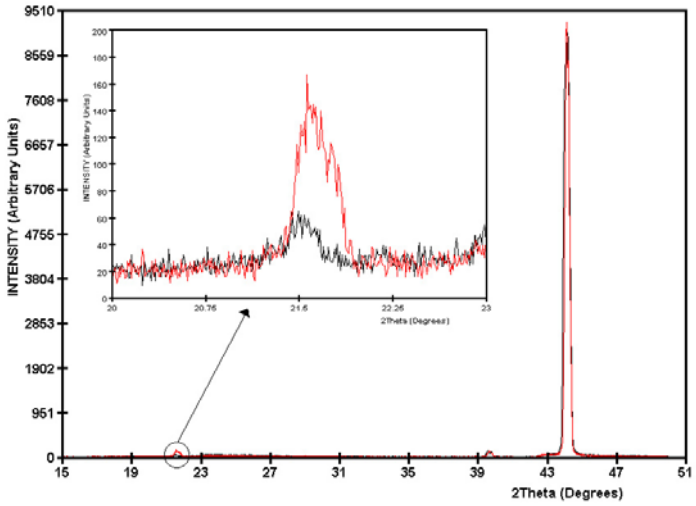

Figure 2.4. *2θ scan for the (χ,φ) = (44.5,270.5) (black) and (38.6,-5.3) positions (red).*

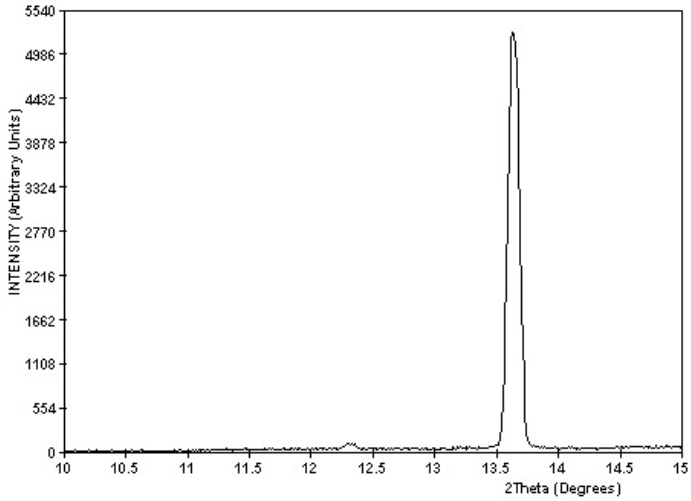

Figure 2.5. *2θ scan of (200) at (χ,φ) = (0,0).*

Finally, when the planes perpendicular to the ***a*** direction were polished, we performed 2θ scan, (200), at $\chi = 0$ and $\varphi = 0$ to confirm the orientation of the sample, as it is shown in Figure 2.5. These confirm that the ***a*** direction was perpendicular to its corresponding polished face.

2.3. Concentration measurements of dopant elements: Electron Probe Microanalyses (EPMA).

The dopant concentration in the crystals was measured by Electron Probe Microanalysis (EPMA). This non-destructive technique uses a focused electron beam to produce characteristic X-rays from the sample. These are used to determine the chemical composition of very small regions in solid samples. In routine analysis, electron microprobe detection limits are about 100 ppm.

We used a Cameca SX-50 Microprobe Analyser (see Figure 2.6) operating in wavelength dispersive mode at 20 kV accelerating voltage and 30 nA beam current for Rb, Ti, P, O and Nb and 100 nA for Er, Yb and W. It is available at the *Servei de Recursos Científico-Tècnics* of the University of Barcelona (Spain). The wavelength-dispersive spectrometer (WDS) comprises a crystal monochromator and an X-ray detector arranged in such a way that X-rays that impinge on the crystal are diffracted according to Bragg's law and only those in a narrow wavelength range reach the detector and are recorded. This selection is made by Rayleigh scattering of the X-rays from a systematic crystal located between the sample and the X-ray detector. The crystals most often used are:

- Lithium fluoride 200 (LIF): ionic solid, $2d = 4.028$ Å
- Pentaerythritol 002 (PET): organic crystal, $2d = 8.742$ Å
- Thallium acid phthalate 1011 (TAP): organic crystal, $2d = 25.75$ Å
- PC1: multilayered pseudo-crystal consisting of many alternating layers of W and Si, $2d = 60$ Å.

By using these crystals the wavelength range covered 1-24 Å. This means that we could record *K*-lines for elements with atomic number (*Z*) between 9 and 35, *L*-lines for elements with *Z* less than 83 and all *M* lines. This technique is highly sensitive to the detection of low elements such as Be, B, C, N, O and F, but the measurement error is high.

Quantitative analysis requires making corrections to the raw data such as deadtime, background and instrumental drift, before making the matrix corrections for inter-elements effects. The corrected intensity ratio of an element's X-ray line is not directly proportional to its concentration because the ratios are affected by X-ray absorption, secondary fluorescence, electron backscattering and the electron stopping power of the sample. There are several methods to take these factors into account and determine concentrations. We used PAP,[162] which uses fundamental factors to correct the effects of atomic number, absorption and fluorescence.

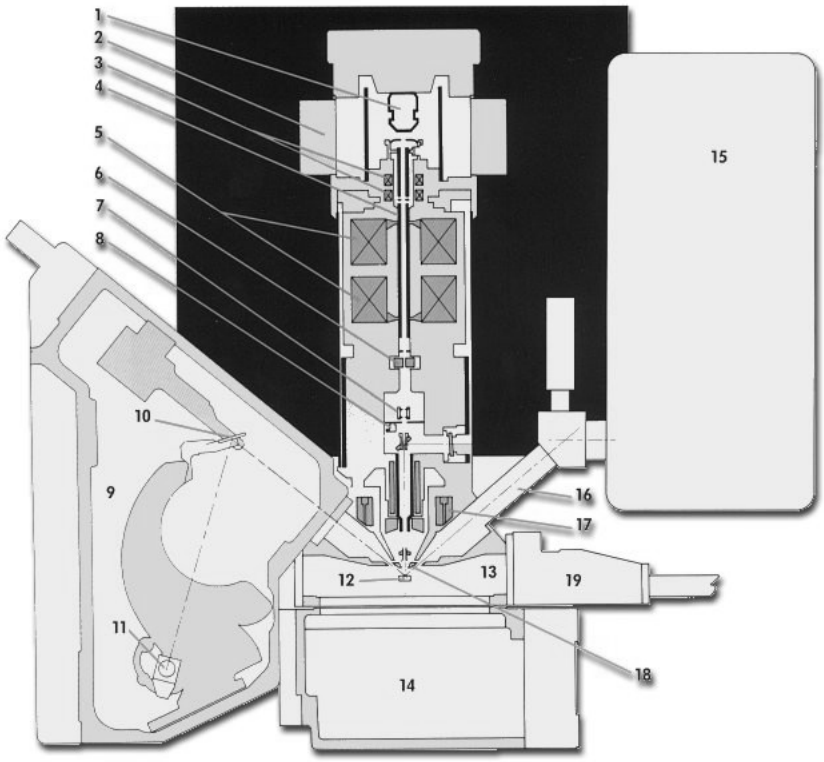

1. Cathode
2. Ionic pump
3. Alignment bobbin
4. Electrons absorbent
5. Condensor lenses
6. Aperture system
7. Electron beam regulator
8. Faraday box
9. Wavelength dispersive spectrometer
10. Diffractor crystal
11. Proportional counter
12. Sample
13. Chamber
14. Sample control
15. Energy dispersive spectrometer
16. EDS aperture
17. Final lenses
18. Retrodispersed electron detectors
19. Vacuum pre-chamber

Figure 2.6. *Schematic diagram of an electron microprobe.*

Owing to the mechanical nature of the spectrometer and to fluctuations in the density of the counter gas detector, the efficiency of WDS may change over time and therefore, need re-calibration. This makes it difficult to use WDS in standardless analysis. We used the standards detailed in *paper II*.

Paper II also describes how we prepared the samples for analysis. Table 2.1 summarises the conditions of analysis.

Table 2.1. *Measurement conditions used in EPMA analysis.*

Element	Line	Time (s)	Spectrometer crystal	Standard	Detection limit (wt%)	Experimental error (%)
Rb	L_α	10.0	TAP	$RbTiOPO_4$	0.05	1
Ti	K_α	10.0	PET	$RbTiOPO_4$	0.02	1
P	K_α	10.0	TAP	$RbTiOPO_4$	0.02	1
O	K_α	10.0	PC1	$RbTiOPO_4$	0.15	3
Nb	L_α	60.0	PET	$LiNbO_3$	0.06	3
Er	L_α	60.0	LIF	REE1	0.02	4
Yb	L_α	60.0	LIF	YbF_3	0.09	3

We paid special attention to determining the experimental error (ε) of the measurements for all the analysed elements, particularly those with a low concentration typical of traces. To do this we used the following expression:

$$\varepsilon = \sqrt{\frac{I_p/t_p + I_b/t_b}{\left(I_p - I_b\right)^2} + \frac{I_p^s/t_p^s + I_b^s/t_b^s}{\left(I_p^s + I_b^s\right)^2}} \times 100 \qquad \text{Eq. 2.1}$$

where I_p is the intensity of the peak in the sample in counts per second (c/s), I_b is the intensity of the background of the sample (c/s), t_p is the integration time of the peak of the sample in seconds (s), t_b is the integration time of the background of the sample (s), I_p^s is the intensity of the peak in the standard (c/s), I_b^s is the intensity of the background of the standard (c/s), t_p^s is the integration time of the peak of the standard (s) and t_b^s is the integration time of the background of the standard (s).

We also determined the detection limits of this technique for all the elements analysed using the following expression:

$$DL = \left[\frac{C^s}{\left(I_p^s - I_f^s\right)}\right] 3\sqrt{2}\left(\frac{I_f}{t_f}\right)^{1/2} \qquad \text{Eq. 2.2}$$

where C^s is the concentration of analyte in the standard in weight per cent (wt%). The results are also given in Table 2.1.

2.4. Microscopy techniques.

In this Section we describe the main characteristics of the microscopy techniques we used to observe the surfaces of the crystals.

2.4.1. Reflection Optical Microscopy.

Reflection optical microscopy is based on the normal incidence of visible light in the sample and the simultaneous normal visualization of this sample through an objective. This particular configuration of the paths of the incident and reflected beams gives the reflected image a high level of illumination. This makes it easy to visualise the sample and provide a high contrast in the observation

of the details. In this study we used Olympus BH-2 and Olympus TL-2 microscopes. These are available at the FiCMA.

2.4.2. Scanning Electron Microscopy (SEM).

The scanning electron microscope (SEM) is used in several fields such as materials development, metals, ceramics and semiconductors. Using the SEM, not only can we observe very fine details (high resolution) but we can also focus on a wide range of specimen surfaces (large depth of field).

The technique involves scanning a surface with a thin electron beam generated in a collimator column. When an electron beam impinges on a specimen, it is scattered by atomic layers near the surface of the specimen. As a result, the direction of the electron motion changes and its energy is partially lost. Quanta generated (secondary electrons, backscattered electrons, X-rays and so on) carry information that describes the nature of the specimen (its atomic number, elemental distribution, topography, surface potential distribution, magnetic domain, chemical and crystallographic characteristics, etc.). This information is converted into a video signal and displayed on a CRT as a scanning image. This technique can obtain between 20 and 30,000 magnifications.

In this study we used a Jeol JSM 6400 electron microscope. Before observation, the samples were gold-sputtered with a Bal-Tec SCD004 sputterer. Both the microscope and the sputterer are available at the *Servei de Recursos Científics* of the Rovira i Virgili University.

2.4.3. Atomic Force Microscopy (AFM).

The Atomic Force Microscope (AFM) is one of about two dozen types of scanned-proximity probe microscopes. All of these microscopes work by measuring a local property, such as height, optical absorption or magnetism, with a probe or tip placed very close to the sample. The small probe-sample separation enables measurements to be taken over a small area.

The concept of resolution in AFM is different from radiation-based microscopies because AFM imaging is three-dimensional. AFM can achieve a resolution of 10 pm and, unlike electron microscopes, it can image samples in both air and in liquids.

The principles behind AFM work very simple. An atomically sharp tip is scanned over a surface with feedback mechanisms that enable the piezo-electric scanners to maintain the tip at a constant force (to obtain height information) or height (to obtain force information) above the sample surface. AFM operates by measuring attractive or repulsive forces between a tip and the sample. In its repulsive or contact mode the AFM measures the local sample height. In its attractive or non-contact mode the AFM derives topographic images from measurements of attractive forces; the tip does not touch the

sample. The tapping mode overcomes problems caused by friction, adhesion, electrostatic forces and others of conventional AFM scanning methods by alternately putting the tip into contact with the surface to provide high resolution, and then lifting the tip off the surface to avoid dragging it across the surface. This mode allows high-resolution topographic imaging of sample surfaces that are easily damaged, loosely held to their substrate or difficult to image by other AFM techniques.

Unlike SEM, AFM provides extraordinary topographic contrast, direct height measurements and unobscured views of surface features. This is because no coating is necessary. We used the AFM available at the University of Utrecht (The Netherlands).

2.5. Differential Thermal Analysis (DTA).

Thermal analysis comprises several techniques in which a physical property of a substance is measured as a function of temperature while the substance is subjected to a controlled temperature programme. When a material is heated or cooled, its structure and chemical composition can undergo changes such as fusion, melting, crystallisation, oxidation, decomposition, reaction, transition, expansion and sintering. These changes can be observed by thermal analysis.

Differential Thermal Analysis (DTA) measures the temperature, direction and magnitude of thermally induced transitions in a material by heating or cooling a sample and comparing its temperature to the temperature of an inert reference material under similar conditions. This difference in temperature is determined as a function of time or temperature in a controlled atmosphere and provides useful information about the temperatures, thermodynamics and kinetics of reactions. This technique is sensitive to endothermic and exothermic processes including phase transitions, dehydratation, decomposition and redox or solid-state reactions.

Thermogravimetric analysis (TGA) determines the weight gain or loss of a condensed phase due to gas release or absorption as a function of temperature in a controlled atmosphere. This technique is useful for determining the purity of the sample, the content of water and carbonate, and the organic content. It is also useful for studying decomposition reactions.

In the combined DTA-TGA system (simultaneous thermal analysis: STA) both thermal and mass change effects are measured at the same time on the same sample. We used an SDT 2960 analysis instrument from TA Instruments, available at FiCMA, operating between room temperature and 1773 K. This information differentiates between endothermic or exothermic events that have no associated weight change (e.g. melting and crystallisation) and those that have (e.g. degradation). The accuracy and precision of this device are given in Table 2.2.

Table 2.2. *Accuracy and precision of the measurements taken with the SDT.*

Temperature accuracy	± 1 K
Temperature precision	± 0.5 K
Weight sensitivity	0.1 μg
Weight accuracy	± 1%
ΔT sensitivity	0.001 K

2.6. Diffraction techniques.

2.6.1. X-ray diffraction techniques.

Much of what we know about the architecture of molecules is derived from studies on the diffraction of X-rays by crystals. This method was first used by W.L. Bragg in 1913. Since then, X-ray and neutron diffraction have helped to establish detailed features of the molecular structure of every kind of stable chemical species in a crystalline form, from the simplest to those with many thousands of atoms.[163]

2.6.1.1. X-ray powder diffraction.

In the summer of 1913, W.L. Bragg showed that scattered radiation from a crystal behaves as if the diffracted beam was "reflected" from a plane passing through points of the crystal lattice in a way that makes these crystal-lattice planes analogous to mirrors. From such considerations Bragg derived the famous equation that now bears his name:

$$n\lambda = 2d_{hkl}\, sin\, \theta \qquad \text{Eq. 2.3}$$

where λ is the wavelength of the radiation used, n is an integer (analogous to the order of diffraction from a grating so that $n\lambda$ is the path difference between waves scattered from adjacent lattice planes with equivalent indices), d_{hkl} is the perpendicular spacing between the lattice planes in the crystal and θ is the complement of the angle of incidence of the X-ray beam.[163]

With a powdered crystalline specimen, many different orientations of tiny crystallites are present simultaneously. For any set of crystal planes, Bragg's law will be satisfied in some of the crystallites, so the complete diffraction pattern will be observed for any orientation of the specimen with respect to the X-ray beam.[163] Powder diffraction is an extremely powerful non-destructive tool

for identifying crystalline phases and qualitatively and quantitatively analysing mixtures. It is used to analyse unit-cell parameters as a function of temperature and pressure and to determine phase diagrams. Compilations of common powder diffraction patterns are maintained by the Joint Committee for Powder Diffraction Standards (JCPDS).[163]

However, in powder diffraction, we lose the 3-dimensional information we can obtain from single crystals. This makes it much harder to solve structures by powder diffraction alone. However, sophisticated methods, originally introduced by H.M. Rietveld in 1967,[164] give precise unit-cell dimensions, atomic coordinates and temperature factors for adjusting parameters with an experimental powder diffraction pattern. This is of course invaluable when suitable large crystals cannot be grown.[163]

We used a Siemens D-5000 powder diffractometer with Bragg-Brentano parafocusing geometry and a θ-θ configuration, using a Cu source ($K_{\alpha 1}$; λ_1 = 1.540560 Å and $K_{\alpha 2}$; λ_2 = 1.544390 Å), available at the *Servei de Recursos Científics* of the Rovira i Virgili University. In this system, the source, the detector and the sample are oriented in the same direction and occupy three consecutive positions on a circumference. This configuration guarantees the same Bragg conditions for a large area of the sample. The positions of the source and the detector vary in a synchronous way, always maintaining a symmetrical position, while the sample is always fixed. In this way we obtain a discrete pattern of the reflections for the families of planes that are parallel to the surface of the sample when the source and the detector take on different 2θ angles.

In the thermal characterisation we incorporated an Anton-Paar HTK10 platinum ribbon heating stage. This was connected to a thermocouple and, to allow different velocities for heating and cooling the sample, to a controller.

2.6.1.2. X-ray single-crystal diffraction.

X-ray single-crystal diffraction is still the method of choice for determining structures. It is used to determine the basic geometry (the space group and lattice parameters) of individual crystals, their structure and the positions of the atoms in the lattice.

The X-ray diffraction pattern of a crystal, which is mainly the result of the X-rays diffracted by the electrons of the atoms, is the sampling at the reciprocal lattice points of the X-ray diffraction pattern of the contents of a single unit cell. Analysis of the diffraction angles produces an electron density map of the crystal. It is only necessary to find the atomic arrangement in one unit cell, which can be derived from the overall intensity variation in the diffraction pattern, and then repeat it according to the direct lattice to give the entire crystal structure. The spatial arrangement of the diffracted beams is determined by the geometry of the crystal lattice and the intensities are determined by the arrangement of atoms within one unit cell.[163]

Data collection (the result of a systematic rotation of the single crystal with respect to the X-ray beam) produces a complete set of data comprising a list of peak positions (*hkl* indices of the reflections) and the corresponding intensities. A first electron density map is calculated from these results, the mathematical refinement techniques are used to improve the approximate atom coordinates obtained from the imperfectly phased Fourier synthesis. Refinement obtains final coordinates and, for each atomic position, a displacement or thermal parameter. The geometry of the molecule (bond lengths, valence and torsion angles) can be derived from the atomic coordinates. Information about the intramolecular forces that stabilise the various molecules can also be derived by analysing the crystal packing.

We used a CAD4 Enraf-Nonius diffractometer, available at the *Servei de Recursos Científico-Tècnics* of the University of Barcelona, with a Mo monochromatic radiation. This is a four-circles diffractometer that can be used to do three different rotations of the crystal.

2.6.2. Neutron powder diffraction.

Since they first appeared as an experimental technique in 1950, neutrons beams have been used to complement intense sources of X-rays.

The scattering of neutrons is a nuclear phenomenon. Whereas X-ray scattering factors increase strongly as the atomic number increases, neutron scattering factors vary much less and do not depend on the angle. As a result, neutron diffraction is not dominated by the heavy atoms present in the molecule. Atoms whose atomic numbers are similar (almost undistinguishable in X-ray diffraction) may have significantly different neutron scattering factors, because there is a magnetic diffraction of neutrons as well as the nuclear diffraction of neutrons. Unlike photons (X-ray diffraction), neutrons have a magnetic moment due to their spin, which can couple with the magnetic field of ions in some crystals and modify the diffraction pattern.

Neutrons are produced by fission reactions in a nuclear reactor or by irradiating a metal target with high-energy protons from an accelerator. This is called spallation. Reactor sources produce a continuous spectrum of neutron energies and require a monochromator crystal to select a particular energy. Accelerator sources are usually operated in a pulsed mode and neutron wavelength is selected by time-of-flight methods, i.e. from data taken at a fixed Bragg angle as a function of neutron energy.

In this study we used the D2B high-resolution powder diffractometer of the Institute Max von Laue – Paul Langevin in Grenoble (France). This diffractometer, which is described in *paper III*, is characterized by a very high take-off angle (135º) for the monochromator. It is 300 mm high and focuses vertically onto about 50 mm. This large-incident vertical divergence is matched by 200 mm high detectors and collimators. A complete diffraction pattern is obtained after about 100 steps of

0.025º. Such scans usually take 30 minutes and are repeated to improve statistics. The diffractometer uses Debye-Scherrer geometry with the detector in the horizontal plane. The D2B diffractometer is particularly well suited for the Rietveld refinement of relatively large structures of less than 2000Å and uses wavelengths of between 1.051 Å and 6Å.

2.7. Spectroscopic techniques.

In this Section we analyse the fundamentals of the spectroscopic techniques we used in this Thesis.

2.7.1. Absorption and transmission measurements.

Absorption is the energy extracted from the electromagnetic wave and transformed into another type of energy when the electromagnetic wave passes through the material.

The absorption coefficient (α) is the variation in the intensity of the electromagnetic radiation through a medium and is represented by the following expression:

$$I = I_0 e^{-\alpha d} \qquad \text{Eq. 2.4}$$

where I_0 is the intensity of the incident light and d is the thickness of the sample.

The absorption is reflected in the variation of the intensity of the electromagnetic radiation, which is determined as a function of the wavelength. To measure this absorption we can measure the optical density (*DO*) with a double ray spectrophotometer:

$$DO = -log(I/I_0) = log(I_0/I) \qquad \text{Eq. 2.5}$$

If we combine equation 2.4 and 2.5, we can correlate α and *DO*:

$$\alpha = DO\left(\frac{1}{d\ log\ e}\right) \qquad \text{Eq. 2.6}$$

We can also correlate α with the absorption cross-section (σ) of every absorbing atom or ion:

$$\sigma = \frac{\alpha}{N} \qquad \text{Eq. 2.7}$$

where N is the density of absorbent centres. In this expression, α is given in cm^{-1} and N in $atoms \cdot cm^{-3}$. Therefore, σ has units of $atoms \cdot cm^2$ or simply cm^2.

Absorption studies were carried out in a Varian Cary 500 Scan spectrophotometer, available at the FiCMA. This is a double ray spectrophotometer with an effective spectral range from 0.25 to 3.00 μm and allows us to measure optical densities from 0 to 10. This spectrophotometer has two monochromators that can separate 1200 lines/mm in the UV-visible region and 300 lines/mm in the IR region. The light is detected by a photomultiplier in the UV-visible region and a lead sulphide in the IR region. The light sources of the spectrophotometer are a deuterium lamp in the UV region and a quartz halogen source in the visible-IR region. We also used a Perkin-Elmer Lambda 900 Spectrophotometer operating in the same region, available at the *Laboratoire de Physico-Chimie des Matériaux Luminescents*, of the Claude Bernard University in Lyon (France).

To study the optical absorption at low temperatures (6 K), we used a Leybold helium closed circuit cryostat. The same cryostat has a controlled heater that can stabilise the temperature in the 6-100 K range with a precision of ± 3 K and in the 200-300 K range with a precision of ± 5 K.

We used the same spectrophotometer to measure the transparency in the UV-visible and NIR region. In the IR region we used an FTIR Midac Prospect spectrophotometer in the 3.0-10.0 μm region. This is available at the *Servei de Recursos Científics* of the Rovira i Virgili University.

When we expected differences due to the polarisation of the incident beam, we used a Glan-Thompson quartz polariser, located before the sample, to eliminate any polarisation induced by the optical components of the spectrophotometer and ensure that we were working only with a polarised component of the incident light.

In all experiments we set an aperture diameter to ensure the measurement beam was absorbed or transmitted with no crystal-edge obscuration. A reference measurement was taken before the crystal sample was placed in the beam path. The sample was mounted with one of the fundamental crystal axes parallel to the electric field of the incident beam and placed at the slit image position located at the midpoint of the beam path in the measurement compartment. The wavelength range was sampled at 0.03-0.5 intervals with a 0.06-2 nm system bandwidth, depending on the wavelength range and the intensity of the multiplet. For IR spectra, each measurement comprised an average of 32 consecutive spectra sampled with a 4 cm^{-1} system bandwidth.

2.7.2. Luminescence measurements.

Optical emission, or luminescence, is the result of a radiative transition of an electron from an excited level or a higher energy level to a lower energy level, which is normally called the ground level. The temporal evolution of the luminescence after the excitation of the electron is an exponential

decline in the intensity of the emission over time. The time between the start of the emission and the time when its intensity decreases to 1/*e* of its initial value is called the radiative lifetime (τ). This is an important parameter which characterises how an electronic level is depopulated and characterises the thermalisation mechanisms of this excitation.

The emission spectra are obtained by fixing the excitation wavelength and changing the detection wavelength. Determining the radiative lifetimes, requires a pulsed excitation source, with pulses shorter than the mean lifetime of the energetic levels of the ion we would like to study in a certain material.

In this study, we obtained the emission spectra by exciting the samples with a BMI VEGA Optical Parametric Oscillator (OPO) pumped by a BMI SAGA seeded YAG:Nd^{3+} laser available at the FiCMA. The laser and the OPO deliver excitation pulses of 7 ns in duration and a repetition rate of 10 Hz. The fluorescences were analysed spectrally with a HR460 Jobin Yvon-Spex monochromator. This, had a focal length of 460 mm and a spectral resolution of 0.05 nm. The fluorescences were detected by a cooled Hammamatsu R5509-72 NIR photomultiplier. The luminescence signal was analysed by an EG&G 7265DSP lock-in amplifier. The radiative lifetime was measured with a computer-controlled Tektronik TDS-714 digital oscilloscope. We also used a Laser Analytical Systems -dye laser, available at the *Laboratoire de Physico-Chimie des Matériaux Luminescents* of the Claude Bernard University in Lyon. In this case, the fluorescence was analysed with an HPS 2 Jovin Yvon monochromator, and detected by a Hammamatsu R1767 photomultiplier. The luminescence signal was analysed with a Standford Research systems SR250 Boxcar Integrator and the radiative lifetime was measured with a LeCroy 9400 digital oscilloscope.

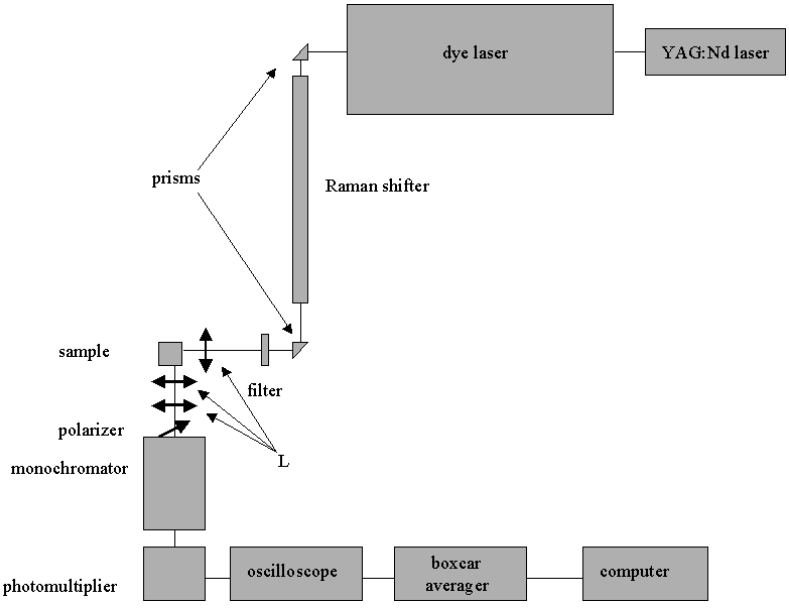

Figure 2.8. *System used to measure luminescence in the Laboratorie de Physico-Chimie des Matériaux Luminescents of the Claude Bernard University.*

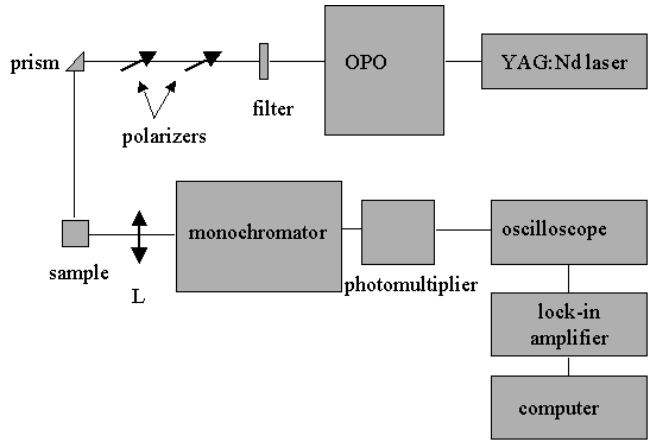

Figure 2.9. *System used to measure luminescence in the Laboratori de Física i Cristal·lografia de Materials of the Rovira i Virgili University.*

2.7.3. Site Selective Spectroscopy.

The structural sites occupied by lanthanides can be studied by measuring the luminescence of intraconfigurational $4f^n$ transitions. The sharp lines corresponding to the $4f^n$-$4f^n$ transitions show small, but significant shifts depending on the type of coordination.

We obtained steady-state site-selective emission and excitation by exciting the sample with a Ti-sapphire ring laser (0.4 cm^{-1} linewidth) in the near infrared, 780-920 nm range available in the *Departamento de Física Aplicada I* of the Basc Country University in Bilbao (Spain). Fluorescence was analysed with a 0.22 m Spex monochromator and the signal was detected by an extended infrared Hamamatsu R928 photomultiplier. Finally, the signal was amplified by a standard lock-in amplifier technique.

2.8. Raman scattering.

Raman scattering is a probe of the vibrational energy levels of molecules. It can immediately provide useful information about the structure and identification of solid, liquid and gaseous substances. The technique is non-contact and non-destructive. It requires minimal sample preparation (in many cases it is not required). Bulk and microscopic materials can be analysed in-situ with high spatial resolution (~ 1 micron). As Raman scattering is different from infrared absorption, these two techniques provide complementary information.

In Raman scattering, a photon is scattered by the molecular system. Most photons are elastically scattered (Rayleigh scattering) and have the same wavelength as the absorbing photon. But in Raman

scattering, the energies of the incident and scattered photons are different because the inelastic scattering of photons by molecules. The energy of the scattered radiation is less than the incident radiation for the Stokes line and for the anti-Stokes line. This increase or decrease in energy is related to the vibrational energy spacing in the ground electronic state of the molecule, so the wavelength of the Stokes and anti-Stokes lines are direct measurements of the vibrational energies of the molecule. The Stokes and anti-Stokes lines are equally displaced from the Rayleigh line because in each case one vibrational quantum energy is gained or lost. Nevertheless, the anti-Stokes line is much less intense than the Stokes line because only molecules that are vibrationally excited prior to irradiation can lead to the anti-Stokes line. In Raman scattering, therefore, only the most intense Stokes line is normally measured.

Since the Raman scattering is not very efficient, we need a high power excitation source. Also, since we are interested in the energy difference between the excitation and the Stokes line, the excitation source should be monochromatic. Raman scattering combined with a conventional optical microscope opens up the possibility of Raman microstructural investigations on the micrometric scale. The experimental set-up we used comprised a Jobin-Yvon T64000 spectrometer with excitation in the visible by a CW argon laser (Coherent INNOVA 300, $\lambda = 514$ nm). Behind the triple-monochromator (1800 $g \cdot mm^{-1}$), the light was detected by a two-dimensional CCD matrix cooled with liquid N_2. A pre-monochromator eliminated the plasma discharge lines of the argon laser. A microscope (Olympus BH2) with high resolution was used to locate the laser spot in the sample. The laser power incident on the sample was about 3.9 mW. We chose a backward scattering scheme in order to increase the signal-to-noise ratio. All this equipment is available at the *Servei de Recursos Científico-Tècnics* of the University of Barcelona.

2.9. Determination of the refractive indexes.

If we want to predict the phase-matching direction with sufficient accuracy, we need to accurately measure the refractive indexes of the non-linear optical materials.

The refractive index is the relationship between the velocity of propagation of an electromagnetic wave in the vacuum and its velocity of propagation in a material. This velocity of propagation depends on the oscillation frequency of the wave, so, the refractive index also depends on this frequency. This effect is called the chromatic dispersion of the light.

We can calculate the real part of the dielectric permittivity of the material, which coincides with the refractive index (n), as follows:

$$n = 1 + \frac{Ne^2\left(\omega_0^2 - \omega^2\right)}{\varepsilon_0 2m\left[\left(\omega_0^2 - \omega^2\right)^2 + \gamma^2\omega^2\right]} \qquad \text{Eq. 2.8}$$

where N is the number of electrons that oscillate in phase, m is the electron mass, ω is the pulsation of the electrons, γ is the extinction coefficient and e is the electron charge. In transparent materials, γ is small and can be neglected. Also, taking into account the relation between the pulsation and the wavelength, we can express the refractive index as a function of the wavelength (λ):

$$n = 1 + \frac{Ne^2\lambda_0^2}{8\pi mc^2\varepsilon_0}\frac{1}{1-\left(\frac{\lambda_0}{\lambda}\right)^2} \qquad \text{Eq. 2.9}$$

where c is the speed of light in vacuum. When λ is far from the resonant wavelength (λ_0), we can simplify the expression by a Taylor development:

$$n = 1 + \frac{Ne^2\lambda_0^2}{8\pi mc^2\varepsilon_0}\left(1 + \frac{\lambda_0^2}{\lambda^2} + \frac{\lambda_0^4}{\lambda^4} + \ldots\right) \qquad \text{Eq. 2.10}$$

From this equation, we can develop the Cauchy equation where, with two constants determined experimentally, we can describe the variation in the refractive index with the wavelength as follows:

$$n = A + \frac{B}{\lambda^2} \qquad \text{Eq. 2.11}$$

However, if the crystal has a strong selective absorption for a certain wavelength range, the experimental chromatic dispersion curve does not adapt to the Cauchy equation in the proximity of this wavelength range. We must then use the Sellmeier expression corrected in the infrared region, taking into account any second resonances at lower frequencies:

$$n^2 = A + \frac{B\lambda^2}{\lambda^2 - C} - D\lambda^2 \qquad \text{Eq. 2.12}$$

In an anisotropic medium, the refractive index is not a unique value. Rather it is different for every spatial direction. We can represent the refractive index as a second order tensor:

$$n_{ij} \equiv \sqrt{\varepsilon_r} \equiv \begin{pmatrix} \sqrt{\varepsilon_{r11}} & \sqrt{\varepsilon_{r12}} & \sqrt{\varepsilon_{r13}} \\ \sqrt{\varepsilon_{r21}} & \sqrt{\varepsilon_{r22}} & \sqrt{\varepsilon_{r23}} \\ \sqrt{\varepsilon_{r31}} & \sqrt{\varepsilon_{r32}} & \sqrt{\varepsilon_{r33}} \end{pmatrix} \equiv \begin{pmatrix} n_{11} & n_{12} & n_{13} \\ n_{21} & n_{22} & n_{23} \\ n_{31} & n_{32} & n_{33} \end{pmatrix} \qquad \text{Eq. 2.13}$$

Using the Onsager theorem,[165] we can justify the symmetric nature of this tensor. We then need only six values to characterise the refractive index tensor. A symmetric matrix can be diagonalised by calculating the eigenvalues, with the principal axes as the eigenvectors. We can therefore describe the refractive index tensor as a diagonal matrix, in which each value represents a principal direction:

$$n'_{ij} = \begin{pmatrix} n'_{11} & 0 & 0 \\ 0 & n'_{22} & 0 \\ 0 & 0 & n'_{33} \end{pmatrix} \qquad \text{Eq. 2.14}$$

This tensor can be assimilated to the Fresnel ellipsoid that can be expressed as:

$$\frac{x^2}{n'^2_{11}} + \frac{y^2}{n'^2_{22}} + \frac{z^2}{n'^2_{33}} = 1 \qquad \text{Eq. 2.15}$$

The coordinates axis of the ellipsoid corresponds to the principal directions and the values of their semiaxes are: $n'_{11} = n_x$, $n'_{22} = n_y$, $n'_{33} = n_z$, which correspond to the eigenvalues of the n_{ij} tensor.

The crystal symmetry gives additional conditions over the symmetric type of the second order tensor and helps to localize the principal axes experimentally by the Neuman principle. For RTP crystals, which crystallize in the orthorhombic system, space group *Pna2₁*, which corresponds to the punctual group *mm2*, the refractive indexes in the principal directions are different ($n'_{11} \neq n'_{22} \neq n'_{33}$) and the principal directions coincide with the crystallographic axes ***a***, ***b*** and ***c***.

We measured the refractive indexes of the samples by the minimum deviation angle method[79,166] with a slight modification. We used semi-prisms of angular directrix $\alpha/2$ and the partial reflection that appeared in the second face of the prism. The angle of the prism was in fact α. Deviation is minimum when the incident and reflected beams are coincident in their paths. We therefore cut two

prisms with an angle of about 22.5º for RTP and for RTP:Nb crystals. Details of this method are explained in *paper IV*.

We measured the variation in the refractive indexes with temperature using the same minimum deviation method in the 293-473 K range at 632.8 nm. The sample was placed in a microfurnace with temperature control and taking care to homogeneously heat the samples. All these experiments were carried out at the FiCMA.

2.10. Non-linear optical characterisation.

After the transparency range and non-centrosymmetry of the material are determined, the next step is to study the non-linear optical (NLO) properties.

Frequency conversion interactions do not involve a transfer of energy to or from the non-linear optical material. The crystal serves only as a medium in which the optical waves can exchange energy between themselves and the incident wave generates a new wave that has a multiple, or harmonic, frequency of the incident wave. It can also generate radiation of two or more frequencies with longer wavelengths that add up to the frequency of the incident field. These processes are used to obtain radiation of frequencies other than those produced directly by lasers. When the light of two frequencies, ω_1 and ω_2, strikes the NLO crystal, there is a non-linear polarisation through the $\chi_{ijk}^{(2)}$ term. One polarisation has the sum frequency ($\omega_1 + \omega_2$). There is also a polarisation at the difference frequency ($\omega_1 - \omega_2$). When the two incident beams have the same frequency and $\omega_1 = \omega_2 = \omega$, the sum frequency generated is 2ω, which is twice that of the fundamental. This is the important process of second harmonic generation (SHG). For this to be effective, the light waves must propagate synchronously, and the velocities and refractive indexes encountered by the interacting waves as they propagate through the medium must match, e.g. $n(\omega) = n(2\omega)$. For phase-matching to occur, there must be an angle of incidence through the crystal at which both the fundamental and second harmonic photons encounter the same refractive index. For SHG, there are two types of phase-matching in the KTP family. In type I, the two fundamental photons are of the same polarisation; in type II, they are orthogonally polarised. Type II is the most efficient type of phase-matching in the KTP family.[66]

2.10.1. Second Harmonic Generation (SHG) efficiency.

We used the powder technique of Kurtz et al.[150] to analyse the SHG properties of these crystals. This is a quick and simple experimental technique that only requires the material in powder form. We

slightly modified the method by detecting both the fundamental and the SHG-generated light in a reflection mode.

Obviously, several simplifying assumptions are needed to reduce a theoretical analysis of SHG in powders to manageable proportions. If the assumptions are sound, rigour can be recovered when more extensive detailed experimental data are available. Kurtz et al.'s[150] basic assumptions made were that the particles were small single crystals of almost identical size, random orientated and that they were densely packed. These assumptions mean that form factors, polycrystallinity and voids are ignored.

Following the assumptions of Kurtz et al.[150] and using the results of Kleinman[167] and Bloembergen,[168] we obtain the following expression for the transmitted second harmonic intensity $I_{ext}^{2\omega}$ in terms of the incident intensity I_{ext}^{ω} (I_{ext} is the intensity external to the slab) for normal incidence:

$$\frac{I_{ext}^{2\omega}c}{8\pi} = \frac{4n_{2\omega}^2}{(n_\omega + n_{2\omega})^2} \times \left[\frac{64\pi l_c d^{2\omega} I_{ext}^{\omega}}{\lambda(n_\omega+1)^2(n_{2\omega}+1)}\right] \times \left\{(1-a)^2 + 4a\,sin^2\left[\left(\frac{\pi}{2}\right)\left(\frac{r}{l_c}\right)\right]\right\} \qquad \text{Eq. 2.16}$$

where n_ω is the index of refraction of non-linear medium at angular frequency ω, l_c is the coherent length defined as $l_c = \frac{\lambda}{4(n_{2\omega} - n_\omega)}$, r is the thickness of the plane-parallel slab, $d^{2\omega}$ is the non-linear optical coefficient ($d_{ijk}^{2\omega}$), λ is the wavelength of the fundamental optical signal, and a is defined as $a = \left[\frac{(n_\omega+1)}{(n_{2\omega}+1)}\right] exp\left[-\left(\frac{\alpha}{2}\right)r\right]$, where α is the absorption coefficient at second harmonic frequency.

As the fundamental beam strikes each particle at normal incidence, after traversing each particle the beam proceeds to the next in line. When travelling through the powder, the beam encounters approximately $L/\hat{r}$ particles, where $\hat{r}$ is the average particle thickness. For particles that are much larger than an average coherence length, the second harmonic fields generated by different particles are assumed to be uncorrelated. In this case, the total second harmonic intensity is just the sum of the contributions from each individual particle. Since each individual particle is assumed to have arbitrary orientation and the fundamental traverses a large number of particles, we can calculate the contribution per particle by performing a suitable average of $I^{2\omega}$ over all angles.

We can therefore obtain the total second harmonic intensity from the powder for $\hat{r} >> l_c$:

$$I_{total}^{2\omega} \cong \frac{32\pi}{c} \times \left(d^{2\omega}\right)^2 \times \left[\frac{64\pi I_{ext}^{\omega}}{\lambda\left(n_{\omega}+1\right)^2\left(n_{2\omega}+1\right)}\right]^2 \times L\frac{\hat{l}_c^2}{\hat{r}} sin^2\left(\frac{\pi\hat{r}}{2l_c}\right) \qquad \text{Eq. 2.17}$$

With phase-matchable materials, such as RTP crystals and their isomorphs, Maker et al.[169] have shown that phase-matching can occur between the polarisation wave. For these directions, the coherence length becomes very large. The angular width over which phase-matching occurs is generally very small, so only a small fraction of the particles are correctly oriented. The major fraction of the angular dependence is now in the coherence length rather than the non-linear coefficient $d^{2\omega}$. In this case, the coherence length can be expressed as:

$$l_c \cong \frac{\lambda}{4\left(n_{2\omega}^{e} - n_{2\omega}^{0}\right)\left(\theta - \theta_m\right) sin\, 2\theta_m} \qquad \text{Eq. 2.18}$$

where n_{ω}^{e} is the extraordinary refractive index, n_{ω}^{0} is the ordinary refractive index at fundamental frequency, θ is the angle between the direction of the fundamental wave and the optic axis and θ_m is the angle between phase-matching direction and the optic axis.

The intensity of SHG is then:

$$I_{ext}^{2\omega} = \left\{\frac{32\pi}{c}\left[\frac{64 I_{ext}^{\omega}}{\lambda\left(n_{\omega}+1\right)^2\left(n_{2\omega}+1\right)}\right]^2\right\} \times \left(d_{PM}^{2\omega}\right)^2 \frac{\pi^2}{4} L\Gamma_{PM} \qquad \text{Eq. 2.19}$$

where $\Gamma_{PM} \equiv \frac{\pi\, sin\,\theta_m}{\beta}$ with $\beta \equiv \left(\omega n_{\omega}^{0} \big/ c\right) sin\,\rho$ and ρ is the angle between the ellipse and the sphere index surfaces at matching. Also, $d_{PM}^{2\omega}$ is that $d_{ijk}^{2\omega}$ for which phase-matching occurs.

Despite this, as we do not know the $d_{PM}^{2\omega}$ of all the crystals, we do not think that the results obtained by the powder method can be taken into account as absolute values. We therefore compared our measurements to those obtained with KTP, the non-linear optical coefficients of which are well known in the literature.[170] Note that in the results we do not take into account the absolute value of $I_{ext}^{2\omega}$. Instead, we used the efficiency of SHG (η), which is defined as:

$$\eta = \frac{I_{ext}^{2\omega}}{\left(I_{ext}^{\omega}\right)^2} \qquad \text{Eq. 2.20}$$

As the sizes of the particles were the same for all the compounds of the KTP family we measured, and as there is little difference in the structures of these compounds, we can use this system to compare our compounds better than when the structure of the compounds is different.

See *paper IV* for a description of how the samples were prepared and the measurements taken.

2.10.2. Determination of the angular non-critical phase-matching directions.

We determined the fundamental wavelength for which phase-matching is along a principal axis of the surface. These interactions are called angular non-critical phase-matching (NCPM) because the associated angular acceptances are the highest. Moreover, the walk-off angle is nil. So, when the corresponding effective coefficient is non-zero for type-II phase-matched SHG, these directions lead to maximal conversion efficiency. We measured this fundamental wavelength of NCPM by directly measuring the phase-matching properties.[171-173] The only initial data needed to perform these measurements is the symmetry class of the material. The crystal, normally cut in a spherical shape, is oriented by X-ray diffraction. It is then placed at the centre of a three-circle Euler goniometric device and illuminated by a fixed laser beam with proper focusing (see Figure 2.9). The method involves rotating the sample on itself in order to propagate the incident beam in different directions and detecting a phase-matching direction when the conversion efficiency is maximum. Instead of a sphere we used a parallellepipedical sample and we used the Euler goniometric circle to ensure perfect autocollimation of the incident wave in the sample.

We developed these measurements in a tunable OPO, Continuum Panther, at a repetition rate of 10 Hz and an FWHM pulse duration of 4 ns. This equipment, which is available at the *Laboratoire de Spectrometrie Physique* of the Joseph Fourier University in Grenoble (France), emits a signal between 0.4 μm and 0.71 μm and the associated idler beam between 0.71 μm and 2.55 μm with a spectral linewidth better than 5 cm^{-1}. We measured the exit wavelength of the OPO in order to avoid calibration problems. This OPO is pumped by a YAG:Nd laser Continuum SLI-10. We used a half-wave plate to adjust the polarisation of the incident beam and ensure the type II phase-matching. With the OPO we could measure the associated spectral acceptance by slightly tuning the fundamental wavelength. This system is shown in Figure 2.9.

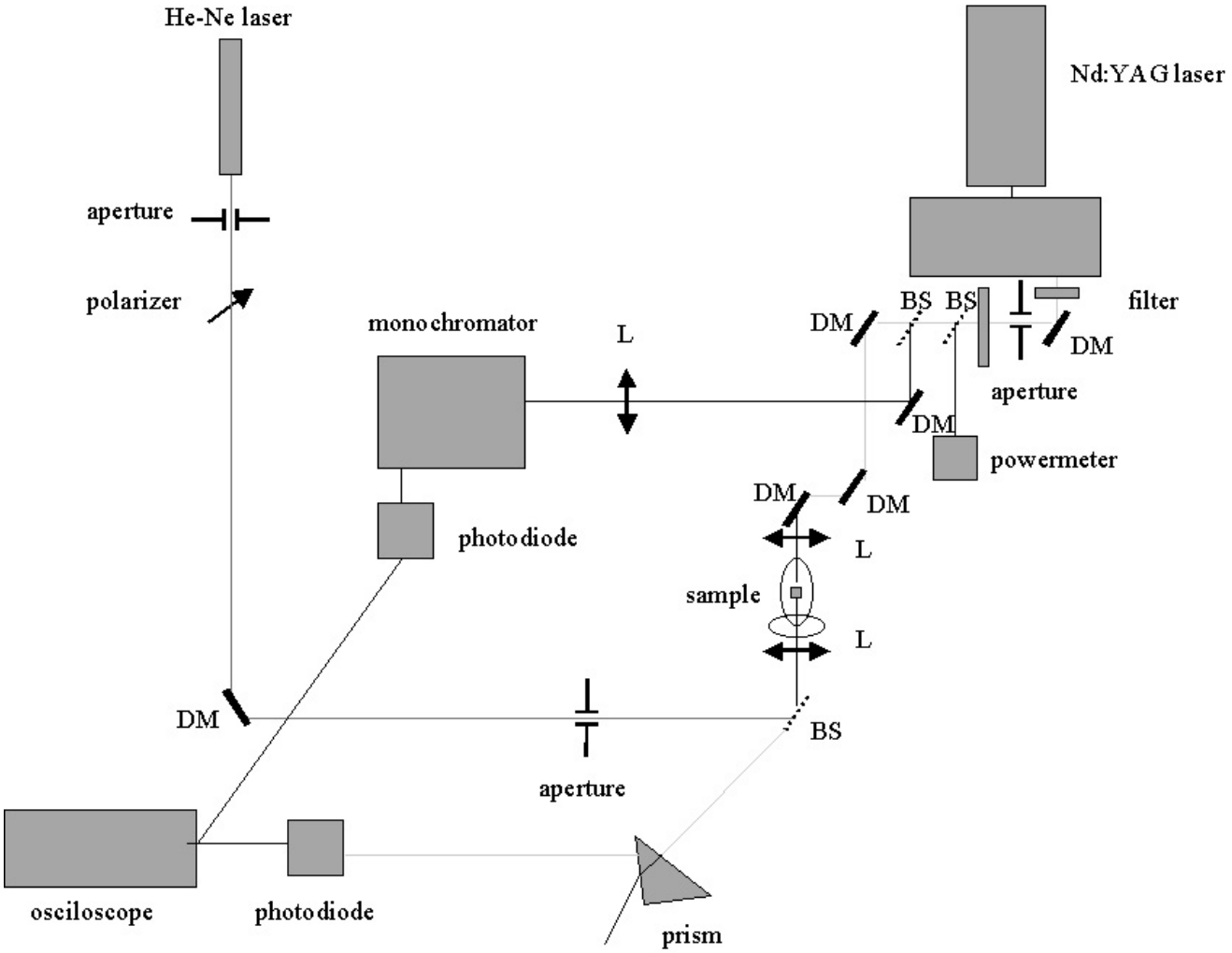

Figure 2.10. *System used to measure the angular non-critical phase-matching wavelengths in the Laboratoire de Spectrometrie Physique of the Joseph Fourier University.*

Initial Page **Table of Contents**